IEEE Access
Multidisciplinary ⋮ Rapid Review ⋮ Open Access Journal

Received 20 April 2026, accepted 6 May 2026, date of publication 14 May 2026, date of current version 19 May 2026.

Digital Object Identifier 10.1109/ACCESS.2026.3693609

RESEARCH ARTICLE

Investigation of Bearingless Partitioned-Stator Flux-Switching Permanent-Magnet Slice Motors

SADJAD MADANZADEH[1], WOLFGANG GRUBER[2], (Senior Member, IEEE), STEFAN MALLINGER[2], (Graduate Student Member, IEEE), RAFAL P. JASTRZEBSKI[3], (Senior Member, IEEE), AND NIKO NEVARANTA[1]

[1]Lappeenranta–Lahti University of Technology, 53850 Lappeenranta, Finland
[2]Johannes Kepler University Linz, 4040 Linz, Austria
[3]University of Turku, 20014 Turku, Finland

Corresponding author: Sadjad Madanzadeh (Sadjad.Madanzadeh@lut.fi)

This work was supported in part by Business Finland under Grant 1803/31/2022; in part by the Linz Center of Mechatronics GmbH (LCM) within the K2 Center for Symbiotic Mechatronics in the framework of the Austrian Competence Centers for Excellent Technologies (COMET) Program; in part by Tohtoristipendi 2021 Säätö ja digitaali; in part by the Academy of Finland under Grant 350880; and in part by the Centre of Excellence in High-Speed Energy Conversion Systems funded by the Research Council of Finland (RCF).

ABSTRACT Flux-switching permanent-magnet machines have gained popularity because their distinctive design places both the permanent magnets and the windings in the stator. This configuration not only improves the structural integrity of the rotor under centrifugal stresses but also makes cooling of the stationary permanent magnets easier and more efficient compared to rotor permanent-magnet structures. These machines are highly versatile and well-suited for applications requiring bearingless motors, including cleanrooms, medical equipment, and pharmaceutical production. However, because the magnetic core must accommodate both the windings and the permanent magnets, it experiences saturation, resulting in performance constraints. This paper proposes a novel bearingless partitioned-stator flux-switching permanent-magnet slice motor architecture. To support this concept, the study focuses on unaddressed challenges in the electromagnetic design of bearingless slice motors, particularly those related to core saturation and the optimization of torque and force performance. By separating the stator into sections containing permanent magnets and copper, iron core saturation is mitigated, resulting in improved torque density. Machine performance is further improved through winding optimization, where various winding schemes are evaluated. The proposed design and underlying principles are validated using 2D and 3D finite-element analyses of the optimized configurations. Experimental validation confirms the theoretical findings, providing a thorough understanding of the operational characteristics of the motor.

INDEX TERMS Flux-switching permanent-magnet motor, partitioned stator, double stator, bearingless motor, self-bearing, magnetic levitation, suspension force, electromagnetic torque.

I. INTRODUCTION

Bearingless motors, also referred to as self-bearing motors, eliminate the need for contact between the rotor and stator frame through the generation of magnetic force and electromagnetic torque. These motors provide multiple benefits, such as contact-free operation, high cleanliness, lubrication-free performance, extended service life with minimal maintenance, low vibration, and a high-speed range, making them ideal for various emerging applications. Additionally, bearingless motors, or those levitated with magnetic bearings, support various configurations, providing one to six degrees of motion freedom for the rotor. Unlike conventional motors with active magnetic bearings (AMBs), bearingless motors integrate the functions of a magnetic bearing and a motor within the same stator/rotor frame,

The associate editor coordinating the review of this manuscript and approving it for publication was Yi Ren.

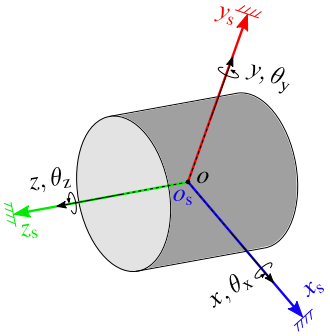

FIGURE 1. Illustration of the rotor in a typical bearingless motor with five DOF for levitation—translations along the x, y, and z axes, and rotations about the x- and y-axes (θ_x and θ_y)—as well as one DOF for rotation about the rotor's main principal axis of inertia (θ_z). The coordinate frame $x_s y_s z_s$ denotes the stator reference frame.

providing one to five axes of active magnetic suspension and torque about the principal inertia axis of the rotor, as shown in Fig. 1 [1].

This paper proposes a novel bearingless slice motor architecture. Prior to presenting the new structure, a comprehensive review and classification of existing bearingless slice motors, focusing primarily on magnet-free rotor designs, particularly flux-switching motors, is provided.

A. BEARINGLESS SLICE MOTORS

Bearingless slice motors are known for their compactness and relatively simple mechanical setup. The flat disc rotor in these motors can be fully stabilized in radial directions through the application of active magnetic forces. Meanwhile, axial and tilting deflections can be passively stabilized through reluctance forces, which result from negative/positive magnetic position stiffness. While these motors are primarily used as pumps in the medical and semiconductor industries, they have also been explored for a variety of other applications such as hermetically sealed process chambers for wafer processing [2], mixers and bioreactors for ultrapure fluid treatment [3], high-speed drives for micro-turbines and compressors [4], blowers or fans for transporting special gases [5], viscometers [6], flywheels [7], and small-scale wind turbines [8].

The concept of a bearingless slice motor with passive stabilization, where the air gap flux is generated by the current flowing through the bearing windings, was first introduced in [9]. A modified design to achieve a more common form with a permanent magnetic biased air gap field was later proposed by [10]. This design has become a cornerstone for several types of slice motors introduced subsequently. These topologies can be categorized based on the type of excitation and further subdivided according to the placement of the magnets relative to the windings, whether they are fixed or moving.

1) Bearingless slice motors with permanent magnet (PM) excitation:
   a) Rotor PM motors: This is the most common type, composed of a rotating PM rotor and a wound stator. Various topologies have been proposed in the literature for bearingless rotor PM slice motors, including standard inner rotor motors [11], standard outer rotor motors [12], segment motors [13], consequent-pole motors [14], high-speed motors with toroidal windings [15], and devices with separated bearing and motor cores [16].
   b) Stator PM motors: These motors incorporate stationary PMs and a wound stator in the same core, forming a type of salient rotor. This category includes bearingless flux-switching/switched-flux PM (FSPM) slice motors [17], bearingless flux-reversal PM (FRPM) slice motors [18], bearingless doubly-saliency PM (DSPM) slice motors, bearingless homopolar-reluctance (HR) slice motors [19], and bearingless hysteresis slice motors [20].
2) Bearingless slice motors without PM excitation: This category, which can be referred to as PM-free slice motors encompasses
   a) Bearingless reluctance slice motors [21], and
   b) Bearingless synchronous reluctance slice motors [22].

Bearingless slice motor drives can also use either separated winding sets, where suspension and torque phases are distinct, or combined winding sets, where each motor phase generates both suspension forces and motoring torque [23].

Rotor PM motors (type 1-(a)) dominate the majority of bearingless slice motors. However, magnet-free rotors are better suited for high-temperature, high-speed applications, and disposable devices. These rotors enhance thermal and mechanical robustness and are a better choice for applications where the rotor must be frequently replaced due to the high cost of rare-earth PMs (type 1-(b) and type 2). On the other hand, PM-type systems (types 1-(a) and 1-(b)) offer higher torque and force densities than motors without PM excitation (type 2). Stator PM motors (type 1-(b)), which show torque density comparable to the more conventional rotor PM motors, are relatively new [24], [25]. These stator PM machines adopt salient poles in the rotor to couple the variation of the PM flux with concentrated stator coils, inducing back electromotive force (back-EMF) and consequently generating torque. Stator PM motors can be designed with either homopolar or heteropolar permanent magnetic air gap flux. Homopolar-type motors generate force comparable with standard bearingless slice motors. However, they suffer from reduced capability in torque generation as only the magnitude of the permanent magnetic field and flux linkage can vary, and its direction cannot change [26]. This issue has been addressed in heteropolar type bearingless slice motors, which can vary according to PM location. In heteropolar stator PM motors, PMs are sandwiched between the teeth in SFPM, attached to the surface of the stator tooth in FRPM, and inserted at the yoke in DSPM.

B. FLUX SWITCHING PERMANENT MAGNET MOTORS

FSPM machines have gained popularity in recent years due to their easier heat dissipation in stationary PMs and performance comparable to conventional permanent magnet machines. This makes them an attractive option for various rotating and linear motor applications. However, to achieve maximum magnetic and electric loading and increase torque density in FSPM, with PMs and copper placed in the same tooth, optimizing the geometry may necessitate reducing stator iron to accommodate PM and copper. Despite the use of multi-tooth, E-core, and C-core topologies in designs, the issue of magnetic saturation in the motor remains inadequately addressed.

In 2015, Evans and Zhu [27] proposed a solution to the problem of conflicting placement of permanent magnets, copper, and stator iron in non-bearingless flux switching permanent magnet machines in the form of a partitioned-stator flux-switching permanent-magnet (PS-FSPM) machine. Placing the magnets in a separate stator prevents core saturation. However, this requires an additional air gap, and the magnetization direction must be reversed to maintain the conventional flux-switching path. This solution, in addition to limiting the saturation in the magnetic circuit, achieves higher torque density, particularly per rotor volume.

C. THE IMPACT AND SIGNIFICANCE OF THE STUDY

Bearingless FSPM motors are relatively new and still not fully explored constructions. For linear applications, they offer a significant material cost reduction by placing the magnets on the mover [28]. For rotating applications, the magnets placed in the stator provide better rotor integrity but result in magnetic forces that have a quadratic current component. Force nonlinearity due to saturation requires nonlinear control, such as proposed in [29]. Modeling, control, commissioning, plant identification, and control design for saturated nonlinear systems are challenging, while performance might still be limited.

This paper advances a bearingless slice partitioned-stator flux-switching permanent-magnet (BS-PS-FSPM) motor by generalizing the earlier concept in [30] to a slice architecture and adding several new elements: a classification-based positioning of the design among bearingless slice motors; a multi-objective electromagnetic optimization (including a study of magnet-volume effects); a comparison of torque/suspension winding schemes for separated and combined systems; and a laboratory prototype with measurements that corroborate the 3D FEM analyses. In contrast to prior publications (including [30]), this work mitigates core-saturation of conventional bearingless FSPM motors through the partitioned stator and provides experimental evidence for torque and suspension force characteristics. To maintain a coherent scope throughout the paper, the present work focuses on proposing the BS-PS-FSPM slice-motor concept and evaluating its electromagnetic performance and passive suspension characteristics. Design-parameter observations, literature-based comparisons, and prototype measurements are included as supporting results that substantiate the evaluation, rather than as separately stated primary objectives. The remainder of the paper first presents the structure and operating principles and briefly frames the role of back-EMF, then details the winding schemes and optimization setup, followed by 2D and 3D FEM analyses and prototype measurements, and finally discusses the results.

II. STRUCTURE AND OPERATION PRINCIPLES

This section introduces the motor structure. It explains the principles behind active and passive stabilizing forces and the unbalanced radial force. Various winding schemes are discussed, and their effects on machine performance are examined.

A. STRUCTURE OF THE PROPOSED BS-PS-FSPM MOTOR

Figure 2 illustrates the structure of the actively controlled 2-DOF BS-PS-FSPM motors with a 12-slot/10-pole configuration. The outer stators could incorporate one or two sets of windings for each tooth, making them suitable for separated, combined, and modular systems. In a separated winding system, the motoring and suspension functions have separate windings, whereas in a combined and modular system, both the motoring and suspension currents share the same coils in each phase. The motoring current is responsible for generating the required electromagnetic torque to rotate the motor in the counter-clockwise direction at an angular velocity of ω_m, while the suspension winding set generates a suspension force in the radial direction. To be more specific, in the proposed bearingless motors, the radial motion of the rotor (x, y) is actively controlled, while the axial (z) and tilting motions (θ_x, θ_y) are passively stabilized through reluctance forces [9]. The inner stator in Fig. 2 is similar to the spoke-type PM rotors found in rotors of PM machines.

In conventional inner rotor FSPM machines, the number of stator slots N_s should be an even multiple of the phase number m; and the rotor pole number N_r should be close to the number of slots N_s, typically differing by ± 2. In PS-FSPM machines, it is possible to explore rotor pole combinations where $N_r = N_s \pm 1$. These variations hold promise for improved performance. However, even with a centralized rotor, the presence of significant unbalance forces renders these odd rotor pole number combinations challenging for bearingless applications. Also, regarding the selection between 12/10 and 12/14 combinations, as shown in [27], although both configurations have the same fundamental order of the cogging torque waveform during an electrical cycle (as given in equation (12) in [27]), the cogging torque in the 12/14 combination is significantly higher than in the 12/10 combination.

In a 2-DOF slice motor, only rotation and radial movements require active control. The application-specific force requirement should be taken into account when optimizing slice motors. Figure 3 illustrates the direction of the

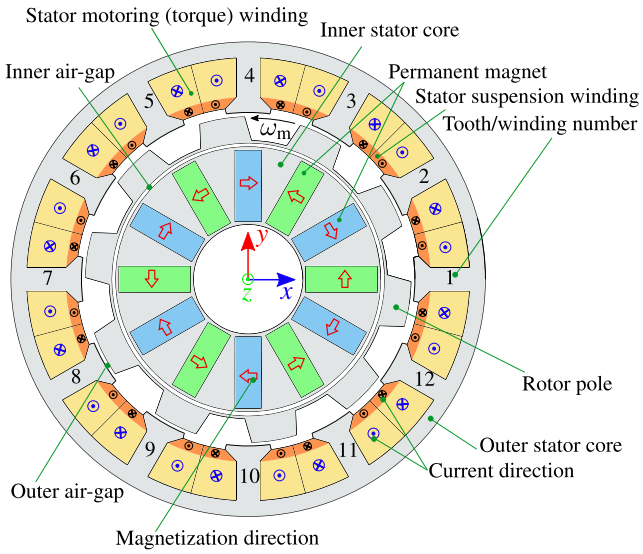

FIGURE 2. Bearingless partitioned-stator flux-switching permanent-magnet slice motor with 12-slot/10-pole configuration. The design allows separated windings in single- and double-layer configurations, as well as combined coils with one coil per tooth to generate both torque and force.

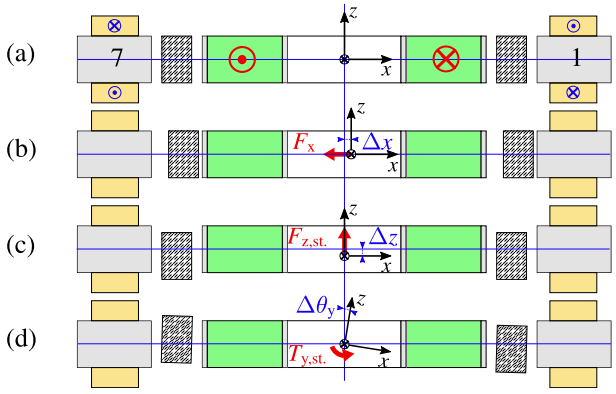

FIGURE 3. Cut-view of the BS-PS-FSPM slice motor illustrating the principle of magnetic suspension force generation: (a) centralized rotor, (b) radial displacement in the x-direction and the active force F_x required to recenter the rotor, (c) axial displacement and the passive stabilizing force $F_{z,st}$ that acts to eliminate the axial deviation, and (d) tilting displacement about the y-axis and the passive stabilizing torque $T_{y,st}$ generated to suppress the angular deviation.

destabilizing force due to rotor eccentricity, as well as the stabilizing force and torque when there is axial displacement and tilting of the rotor of the slice PS-FSPM motor. The passive suspension capabilities of the proposed slice motor can be characterized by the axial stiffness c_z, calculated from the axial force F_z as $c_z(\theta_z) = \mathrm{d}F_z(\theta_z)/\mathrm{d}z$, and the tilting stiffness c_t based on the tilting torque T_t, calculated as $c_t(\theta_z) = \mathrm{d}T_t(\theta_z)/\mathrm{d}\theta_t$. In certain applications, the disturbing axial forces and tilting torques due to the load during motor operation can be high. Conversely, while high values for passive axial and tilting stiffnesses are desired to reduce deflections and improve the stabilization of the rotor, a high value for radial position stiffness, similar to that in active magnetic bearings, leads to negative stiffness effects. The radial position stiffness, defined as the derivative of the radial force with respect to radial displacement, $c_r(\theta_z) = \mathrm{d}F_r(\theta_z)/\mathrm{d}r$, results in a significant destabilizing passive radial force $F_r(\theta_z)$ even for small radial displacements. This destabilizing pull necessitates active radial control currents and force generation to stabilize the rotor.

TABLE 1. Studied winding schemes suitable for PS-FSPM machines with a 12/10 slot/pole configuration (applicable to both separate and combined systems). The torque windings are denoted as U, V, and W (three-phase), and the force winding follows a two-phase scheme labeled A and B.

Coil	1	2	3	4	5	6	7	8	9	10	11	12
TWS1	U	V	W	U	V	W	U	V	W	U	V	W
TWS2	U	U	W	W	V	V	U	U	W	W	V	V
TWS3	U	U	U	U	V	V	V	V	W	W	W	W
TWS4	U	U′	W	W′	V	V′	U	U′	W	W′	V	V′
TWS5	U	U	U′	U′	V	V	V′	V′	W	W	W′	W′
TWS6	U	U′	U′	U	V	V′	V′	V	W	W′	W′	W
FWS	A	B	A′	B′	A	B	A′	B′	A	B	A′	B′

B. WINDING SCHEME

In the design of the proposed bearingless motor, the selection of a winding scheme plays a significant role in overall performance. Table 1 presents six torque winding schemes (TWS1–TWS6) and one force winding scheme (FWS), which can be implemented in both separate and combined winding systems. In Table 1, currents in three-phase UVW and two-phase AB systems can be defined through the following equations.

$$\begin{aligned} i_U &= I_m \sin(\omega t), \\ i_V &= I_m \sin(\omega t - 120^\circ), \\ i_W &= I_m \sin(\omega t + 120^\circ), \end{aligned} \tag{1}$$

$$\begin{aligned} i_A &= I_s \sin(\omega t + \gamma), \\ i_B &= I_s \sin(\omega t + \gamma - 90^\circ), \end{aligned} \tag{2}$$

where ωt represents the rotor electric angle. I_m and I_s denote the peak values of the motoring and suspension currents, respectively, with nominal values given by I_{mn} and I_{sn}. The suspension current angle has values in the range $-180^\circ < \gamma \leq 180^\circ$.

The winding factor influences (proportionally) the flux linkage and the inductances, both of which contribute to torque and force production. The combinations of stator slots and rotor poles, together with the winding scheme, affect the winding factor while shaping performance and efficiency. The winding factor, for the ν-harmonic, $k_{w,\nu}$ is the product of the distribution factor $k_{d,\nu}$ and the coil pitch factor $k_{p,\nu}$ [31], such that

$$k_{w,\nu} = k_{d,\nu} \cdot k_{p,\nu}, \tag{3}$$

$$k_{d,\nu} = \frac{\sin(\frac{Q\nu\beta}{2})}{Q \cdot \sin(\frac{\nu\beta}{2})}, \tag{4}$$

$$k_{p,\nu} = \cos(\frac{\nu\alpha}{2}), \tag{5}$$

where Q is the number of EMF vectors per phase (which corresponds to the number of slots per pole per phase), β is the angle between two EMF vectors (angular displacement between adjacent slots in electrical degrees), α is the coil pitch angle in electrical degrees (coil span/pole pitch ·180°), and ν is the EMF harmonic. The pole pitch is N_s/N_r. For the concentrated winding, the pitch factor is constant regardless of the winding scheme. Generally, for efficient operation and minimal harmonic distortion, optimal designs try to maximize $k_{w,\nu=1}$ while minimizing $k_{w,\nu>1}$. However, a high winding factor is not a sufficient condition for optimal design for motoring nor for levitation.

The force and torque production is controlled by the suspension and motoring currents as described in the following subsection.

C. FORCE AND TORQUE GENERATING PRINCIPLES

A matrix representation of the radial suspension force equation, at zero rotor radial displacement, can generally be written for all types of bearingless PM motors in the form of a two-phase system [32], as

$$\begin{bmatrix} F_x \\ F_y \end{bmatrix} = c_p K_t \begin{bmatrix} M_1(i_{md}+i_f) & M_2 i_{mq} \\ M_2 i_{mq} & -M_1(i_{md}+i_f) \end{bmatrix} \begin{bmatrix} i_A \\ i_B \end{bmatrix}, \quad (6)$$

where the suspension force components in the x- and y-axes are represented by F_x and F_y, respectively. The PM equivalent field current is represented by i_f. The coefficients related to the derivative of mutual inductances between the motor d-axis and q-axis and radial suspension force windings with respect to the rotor radial displacements are represented by M_1 and M_2, respectively. The d- and q-components of the motoring current in the synchronously rotating reference frame are i_{md} and i_{mq}, respectively. The coefficient c_p is used to apply the effect of the Park transformation when transitioning from a three-phase UVW stationary frame to a two-phase dq rotating frame. The value of c_p is set to 1 when the Park transformation is designed to maintain constant power conversion, and c_p is set to 1.5 when the Park transformation is designed to keep the magnitude of the transferred variable constant. $k_{w,l}$ represents the winding factor for the levitation currents. The transformation matrix K_t, which is used to convert from the suspension rotating to the stationary xy frame, is defined as

$$K_t = \begin{bmatrix} \cos(\omega t) & \sin(\omega t) \\ -\sin(\omega t) & \cos(\omega t) \end{bmatrix}. \quad (7)$$

The electric angular frequency $\omega = N_r \omega_m$. The equation for the electromagnetic torque can be formulated as

$$T_e = c_p N_r \left(\lambda_m i_{mq} + \left(L_d - L_q\right) i_{md} i_{mq}\right), \quad (8)$$

where λ_m represents the flux linkage of the PM rotor and L_d and L_q denote the dq-axis self-inductances. The winding factor $k_{w,m}$ for the motoring currents accounts for the effect of the winding configuration on the generated torque. The effects of the winding configuration are included in the electromagnetic parameters used in (6) and (8), such as the mutual-inductance derivatives, PM flux linkage, and dq-axis inductances. Therefore, the winding factors are not introduced as separate explicit multipliers in these equations.

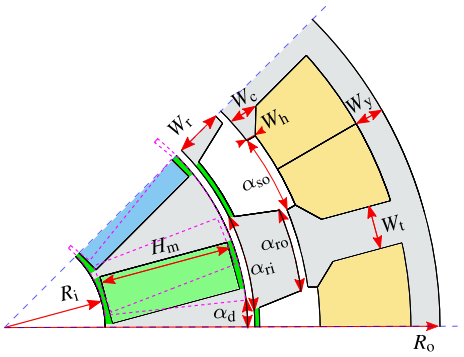

FIGURE 4. Illustration of a partial model of the bearingless slice PS-FSPM motor showing the main geometric parameters.

III. 2D FEM OPTIMIZATION

In the 2D FEM optimization of partitioned-stator flux-switching permanent-magnet machines, the design problem can be approached through either single-objective or multi-objective formulations. For bearingless configurations in particular, the optimization must compromise between torque and levitation performance [33]. This paper focuses on optimizing four distinct parameters within a multi-objective framework using a genetic algorithm (GA). The optimization algorithm is implemented within the FEM-based software JMAG used in this study. The performance indexes include $\overline{T}_e$, measured in Nm, which is the average value of the generated electromagnetic torque T_e, $\tau_{\Delta T}$ that represents the relative ripple of the electromagnetic torque T_e, $\overline{F}_r$, measured in N, which is the average value of the generated radial suspension force amplitude F_r, and $\tau_{\Delta F}$ that represents the relative ripple of the radial suspension force amplitude F_r. The objectives considered are: maximizing $\overline{T}_e$ and $\overline{F}_r$, and minimizing $\tau_{\Delta T}$ and $\tau_{\Delta F}$.

This paper examines two designs: Design 1, which has less permanent magnet volume and is considered a non-saturated design (with initial design $D_{1,i}$ and selected optimum design D_1), and Design 2, which has approximately three times more permanent magnet volume and is considered a saturated design (with initial design $D_{2,i}$ and selected optimum design D_2). Figure 4 displays the key geometric parameters for the bearingless slice PS-FSPM. The optimization process considers eight variables, including the inner radius of the inner stator R_i, rotor radial thickness W_r, magnet height H_m, outer stator tooth thickness W_t, the radial thickness of the pole shoe at the base W_c, the inner angle of the rotor tooth α_{ri}, the outer angle of the rotor tooth α_{ro}, and the slot opening ratio τ_{so} defined as $\tau_{so} = \alpha_{so}/(2\pi - \alpha_{so})$. Table 2 provides the variation range of optimization variables, as well as their values for both the initial and optimized designs. The remaining geometric parameters, along with some electric constants, are defined in Table 3.

TABLE 2. Optimization variables and their ranges of 12/10 configuration.

Parameter	Unit	Non-saturated			Saturated		
		Range	$D_{1,i}$	D_1	Range	$D_{2,i}$	D_2
R_i	mm	[16, 20]	18.0	16.7	[12, 22]	17.3	16.5
W_r	mm	[5, 9]	7.5	7.7	[4, 11]	8.3	7.5
H_m	mm	[10, 25]	20.0	20.7	[15, 30]	22.7	24.9
τ_{so}		[0.2, 0.5]	0.4	0.3	[0.3, 0.7]	0.5	0.3
W_t	mm	[7, 10]	8.0	7.0	[6, 12]	9.0	6.6
W_c	mm	[4, 6]	4.0	4.0	[3, 7]	5.0	3.0
α_{ri}	deg	[6, 12]	10.0	11.9	[6, 12]	10.0	11.4
α_{ro}	deg	[6, 12]	8.0	8.2	[6, 12]	8.0	8.0

TABLE 3. Main optimization constants of 12-slot / 10-pole configuration.

Parameter (Symbol)	Unit	Value
Outer radius of the outer stator (R_o)	mm	75
Deviation angle of the inner stator (α_d)	deg	0
Axial length of the rotor (d_r)	mm	10
Axial length of the stator (d_s)	mm	10
Air gaps (g_0)	mm	1
Thinnest radial thickness of each bridge (W_b)	mm	0.5
Radial thickness of pole shoe in edge (W_h)	mm	1.7
Yoke to tooth thickness ratio ($\tau_{st} = W_t/W_y$)		1.5
Magnet volume for design D_1	mm^3	7200
Magnet volume for design D_2	mm^3	22650
Current density of the coil	A/mm^2	3
Copper filling factor (k_p)		0.4
Copper conductivity (ρ)	Ωm	1.673E-8
Current ratio ($\tau_{amp} = I_m/I_s$)		5
Remanent flux density of NdFeB magnet (B_r)	T	1.2
Electrical steel grade		M330-35A

The motor exhibits different force, torque, and power characteristics for different values of deviation angle of the inner stator α_d, which is set to zero for optimization purposes. However, this parameter can also be considered as an optimization variable, or it can be adjusted after optimization to achieve the desired force, torque, and power features. The stator deviation angle α_d modifies the operating behavior by altering the modulation pattern of the PM flux linkage. For the discrete inner-stator angles $\alpha_d \in \{-30°, -15°, 0°, 15°, 30°\}$, the cases $\alpha_d = 0°$ and $\alpha_d = \pm 30°$ show similar behavior, characterized by an alternating PM flux linkage over one rotor pole, that is, a sign change within a single pole, consistent with the flux-switching operating principle described in this work. Likewise, the cases $\alpha_d = \pm 15°$ have similar behavior to each other, while the required coil energization sequence depends on the direction of the stator shift. Moreover, three geometric constraints given in Table 4 are considered for the optimization. The first constraint limits the outer radius of the rotor, ensuring a reasonable range for the thickness of the outer stator cylinder and, consequently, the depth of the stator slots. The second constraint prevents the internal vertices of neighboring magnets from getting closer than 0.5 mm. The third constraint maintains the slot opening ratio within an appropriate upper limit relative to the tooth width, ensuring that the arc of the tooth shoe is always larger than the arc of the tooth.

TABLE 4. Optimization constraints of 12-slot/10-pole configuration.

no.	Constraint
1	$45\ \text{mm} \le R_i + W_r + H_m \le 53\ \text{mm}$
2	$0.25 \le ((R_i + 0.5)\sin(\pi/N_s) - (0.5S_m/H_m))\cos(\pi/N_s)$
3	$W_t - (R_i + H_m + W_r + 3)\sin(0.5(1 - \tau_{so})\pi/N_s) \le 0$

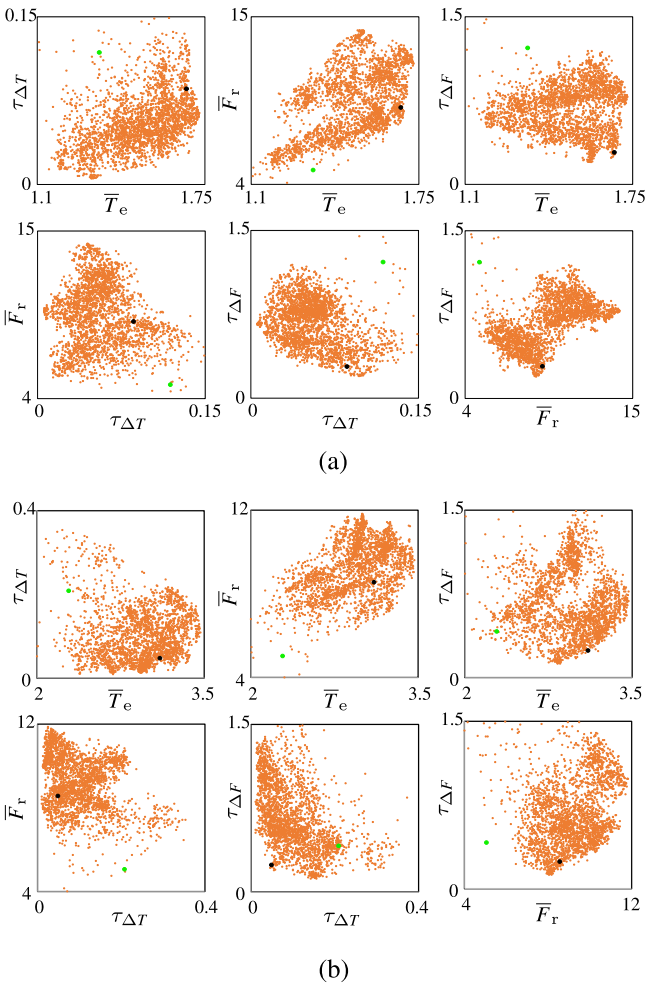

FIGURE 5. Correlation matrix plots for multi-objective optimization: (a) D_1 and (b) D_2, with 2880 cases generated by the GA (•), initial case (•), and selected optimum case (•).

As a basis for the optimization, the copper loss is considered to remain constant for the same phase current. To fix the copper loss for different slot geometries at the same rated current, the phase resistance R_{ph} must be kept constant by applying a relation as $N_{ph} \propto \sqrt{A_s}$ with the number of phase turns N_{ph} and the slot area A_s. Therefore, by applying a constant current density to the slot area, the phase current magnitude and copper loss will change as $I_m \propto \sqrt{A_s}$ and $P_{ohm} \propto A_s$, respectively [27].

Assuming that the geometric limits applied to the slot result in minimal variation in the current range and, consequently, copper losses across different designs, the optimizations were conducted using 2D transient analysis with the JMAG

TABLE 5. Values of objectives in multi-objective optimization of initial and optimized designs obtained from 2D FEM analysis.

Design	$\overline{T}_e$	$\tau_{\Delta T}$	$\overline{F}_r$	$\tau_{\Delta F}$
$D_{1,i}$	1.34	0.12	4.95	1.22
D_1	1.68	0.09	9.06	0.29
$D_{2,i}$	2.29	0.21	5.06	0.42
D_2	3.10	0.05	8.58	0.24

Note: The time interval for averaging is one complete rotation of the rotor.

TABLE 6. Performance factors of different BS-PS-FSPMs featuring 12-slot/10-pole combination with possible winding schemes.

	Criteria	$\overline{T}_e$		$\overline{F}_r$		$\tau_{\Delta T}$		$\tau_{\Delta F}$		$k_{d,1}$
	Design	D_1	D_2	D_1	D_2	D_1	D_2	D_1	D_2	D_1, D_2
Winding Scheme	TFWS1	1.68	3.13	9.06	8.73	0.09	0.05	0.29	0.27	1
	TFWS2	0.91	1.54	7.90	9.98	0.51	0.54	1.15	0.73	0.97
	TFWS3	0.40	0.80	10.5	12.1	0.61	0.57	1.62	1.55	0.84
	TFWS4	1.44	2.73	8.77	8.80	0.16	0.15	0.67	0.49	0.97
	TFWS5	0.76	1.33	9.98	10.6	0.50	0.57	1.70	1.27	0.84
	TFWS6	1.24	2.34	23.6	22.7	0.16	0.14	1.11	1.46	0.84

Note: The background colors dark red (very poor), light red (poor), yellow (moderate), and green (good) represent the performance. TFWSi, the drive-bearing winding scheme, is built by combining the torque winding scheme TWSi and the force winding scheme FWS.

FEM tool. These analyses disregarded iron losses and eddy currents. The used mesh sizes were 1.4 mm in the steel cores, 5 mm in copper, 2 mm for magnets, and 1.2 mm in air.

Figure 5 illustrates selected plots from a correlation matrix that summarizes the outcomes of the multi-objective optimization process. For initial and selected optimum designs with the selected winding scheme (TFWS1), the values of objectives are summarized in Table 5. These plots illustrate the interactions among various parameters, outlining the boundaries of the results achieved through optimization. From regions near the desirable boundary in the objective space, particularly with small $\tau_{\Delta F}$ and large $\overline{T}_e$, two designs are selected for more in-depth analysis. The multi-objective GA used in this study consists of 45 generations and a population size of 64.

IV. DESIGN DEVELOPMENT, ANALYSES, AND DISCUSSION

In developing a BS-PS-FSPM motor, various winding schemes are proposed and evaluated, and the best one is selected as a result of 2D FEM analysis. The electromagnetic performance of the optimized designs is then assessed in 3D FEM, with an experiment provided to demonstrate the concept.

A. SELECTION AND DEVELOPMENT OF WINDING SCHEME

Table 6 summarizes the resulting performance factors obtained from 2D FEM analysis for proposed winding schemes. Comparing these results shows that TWS1 is the best overall motoring winding set for the proposed

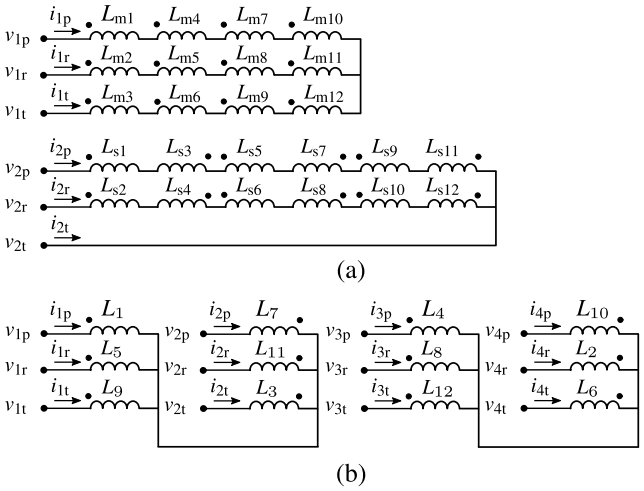

FIGURE 6. Selected winding scheme for the 12-slot/10-pole partitioned-stator flux-switching permanent-magnet motor: (a) separated-winding bearingless motor and (b) combined-winding bearingless motor.

TABLE 7. Allocated voltage and current for 12-slot topology with winding schemes illustrated in Fig. 6.

Combined Winding		Separated Winding	
$v_{1p}, v_{2p} = v_U \pm v_A$	$i_{1p}, i_{2p} = i_U \pm i_A$	$v_{1p} = v_U$	$i_{1p} = i_U$
$v_{1r}, v_{2r} = v_V \pm v_A$	$i_{1r}, i_{2r} = i_V \pm i_A$	$v_{1r} = v_V$	$i_{1r} = i_V$
$v_{1t}, v_{2t} = v_W \pm v_A$	$i_{1t}, i_{2t} = i_W \pm i_A$	$v_{1t} = v_W$	$i_{1t} = i_W$
$v_{3p}, v_{4p} = v_U \pm v_B$	$i_{3p}, i_{4p} = i_U \pm i_B$	$v_{2p} = v_A$	$i_{2p} = i_A$
$v_{3r}, v_{4r} = v_V \pm v_B$	$i_{3r}, i_{4r} = i_V \pm i_B$	$v_{2r} = v_B$	$i_{2r} = i_B$
$v_{3t}, v_{4t} = v_W \pm v_B$	$i_{3t}, i_{4t} = i_W \pm i_B$	$v_{2t} = v_0$	$i_{2t} = i_0$

12-slot/10-pole topology, which provides the unit winding factor, in addition to its other benefits. For a 12-slot/10-pole motor with 12 suspension coils, the two-phase FWS winding scheme is the only viable solution for developing a suspension system for the proposed bearingless motor. It is important to note that a three-phase suspension system with 12 suspension coils cannot generate proper force for this particular slot-pole combination in a partitioned-stator motor. However, a three-phase suspension system with 6 suspension coils can generate the required force for the 12-slot/10-pole motor.

Winding scheme TFWS1 could be practically realized in separate and combined systems. Using separate motoring and suspension windings results in a design with one set of three motoring phases consisting of four coils each and one set of two suspension phases consisting of six coils each as shown in Fig. 6 (a). On the other hand, a combined winding system can be developed with four sets of three phases consisting of one coil, as shown in Fig. 6 (b). Table 7 describes the voltages and currents for the separated and combined winding sets shown in Fig. 6, based on the two- and three-phase systems defined in (1) and (2).

Each one of the two- and three-phase winding sets in Fig. 6 is connected to a power electronic converter with six insulated-gate bipolar transistor (IGBT) half-bridges,

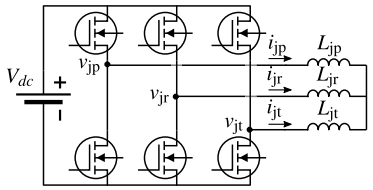

FIGURE 7. Six-switch three-phase inverter.

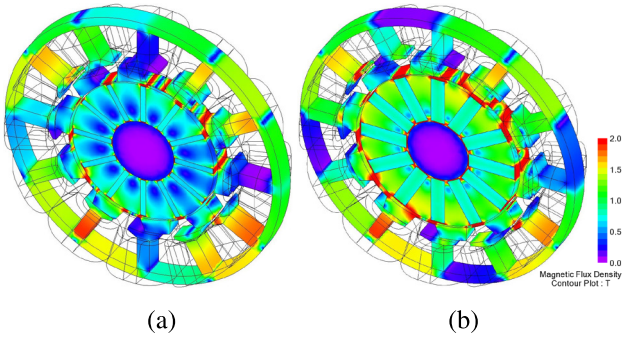

FIGURE 8. Magnetic flux density contour plots for two optimized BS-PS-FSPM motor designs: (a) D_1 and (b) D_2.

as shown in Fig. 7. For the separated winding system, six half-bridges with five current sensors and in the combined winding twelve half-bridges with twelve current sensors are needed to implement the power electronic system. In separated winding, the half-bridge connected to terminal 2t in Fig. 6 (a) is used as the return path for both phases and is operated at 50% duty-cycle. Regarding the number of power electronic devices, it is worth noting that the winding scheme depicted in Fig. 6 (a) is preferable. This could be different in the case of large power motors, e.g. [1], [34], where using multiple phases with shared currents would, generally, lower the DC link voltage and provide better slot utilization leading to lower losses.

B. ELECTROMAGNETIC PERFORMANCE

All FEM results are obtained from 3D analyses, except for the optimization, which is performed using the 2D model. Figure 8 provides a visualization of the magnetic flux density contour plots for the 3D models of two optimized designs, namely D_1 and D_2. In contrast, Fig. 9 illustrates the force orbits obtained from 3D FEM analysis under four distinct scenarios. Each scenario maintains a constant value of I_m and I_s for motoring and suspension currents, respectively, as outlined in (1) and (2). The suspension current angle, however, varies within the range $-180° < \gamma \leq 180°$. Figure 9 demonstrates that the semi-major axes of force-vector ellipses shift by 54°, which is six times (the number of suspension winding poles) the mechanical rotor angle θ_z.

Figure 10 shows the active radial force and the torque generation components for topologies D_1 and D_2. Topology D_2 delivers higher torque than topology D_1 within the same motor volume, almost proportional to their permanent magnet volumes. However, after comparing the results in different

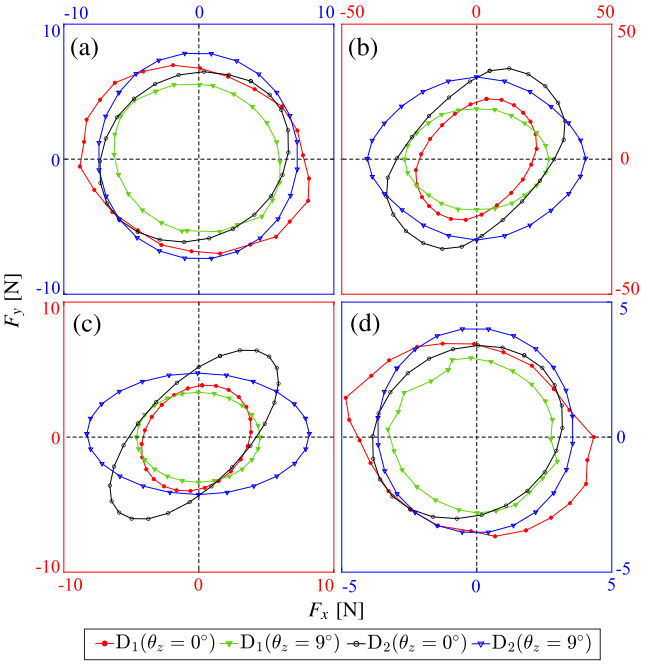

FIGURE 9. Suspension force in x- and y-directions for $\gamma = 0°, 15°, 30°, \ldots, 345°$ for the optimized designs D_1 and D_2 at $\theta_z = 0°$ at (a) $I_m = 11.15$ A and $I_s = 2.23$ A, (b) $I_m = 0$ A and $I_s = 11.15$ A, (c) $I_m = 0$ A and $I_s = 2.23$ A, and (d) $I_m = 11.15$ A and $I_s = 1.115$ A.

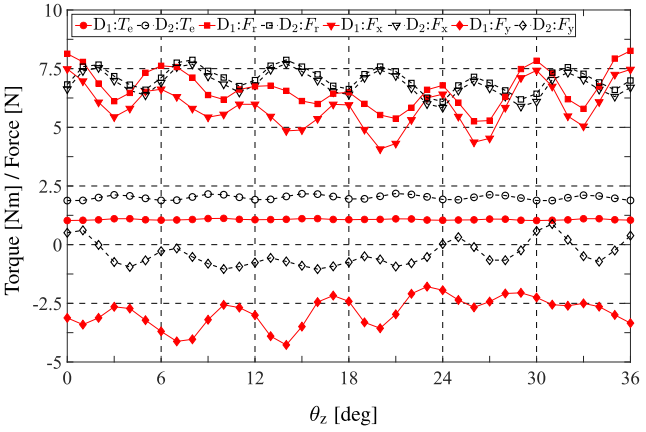

FIGURE 10. Electromagnetic torque T_e and suspension force F_r in x- and y-directions versus rotor angle at nominal motoring current and nominal suspension current with $\gamma = 90°$ for the optimized designs D_1 and D_2.

scenarios in Fig. 9 and examining the results in Fig. 10, it is evident that different values of the motoring coupling parameter M_1 in (6) for designs D_1 and D_2 have had a significant impact on force generation, resulting in nearly identical values for the total radial force in both topologies, specifically at nominal values of motoring and suspension currents.

The 3D results from Fig. 10, when compared with the 2D results, are summarized in Table 8. As can be observed from both 2D and 3D analyses of the optimized cases, the force magnitude does not differ significantly. However, the large volume of the PM in D_2 results in double the

TABLE 8. Performance of optimized designs.

Analysis	Design	$\overline{T}_e$	$\tau_{\Delta T}$	$\overline{F}_r$	$\tau_{\Delta F}$
2D	D_1	1.72	0.134	9.056	0.416
	D_2	3.278	0.166	9.492	0.247
3D	D_1	1.071	0.086	6.645	0.452
	D_2	2.014	0.149	7.071	0.252

Note: The time interval for averaging is one complete rotation of the rotor.

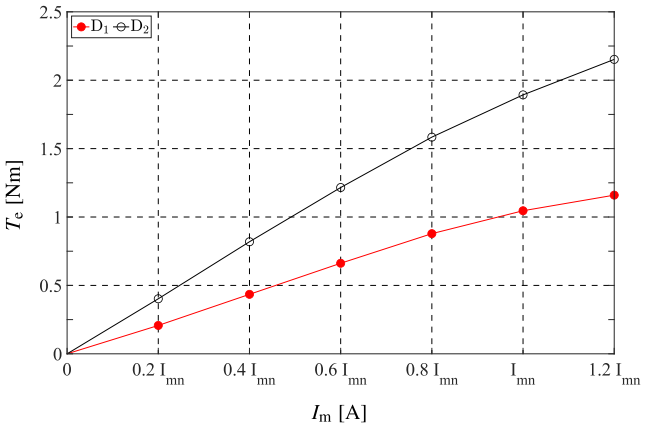

FIGURE 11. Electromagnetic torque T_e at $\theta_z = 0°$ versus motoring current I_m for zero suspension current, $I_s = 0$. The nominal motoring current is $I_{mn} = 11.15$ A.

torque compared to D_1 in both 2D and 3D analyses. It is evident that in slice-type machines, the results of 2D and 3D analyses are not identical due to the disc-shaped structure of the motor, in which flux leakage at the ends constitutes a significant portion of the motor flux. However, relative ripples ($\tau_{\Delta T}$ and $\tau_{\Delta F}$) in 2D and 3D analyses largely match. Therefore, 2D optimization is expected to produce the optimum designs, as good 2D designs are likely to perform better in 3D than weaker ones.

Figure 11 shows the electromagnetic torque resulting from the motoring current when the suspension current is zero. Figure 12 shows the radial force resulting from suspension current when motoring current is zero at $\theta_z = 0°$. The results indicate a predominantly linear relationship between torque and motoring current, as well as between radial force and suspension current. A decrease in torque at higher motoring currents is attributed to saturation effects. As expected, the torque and force coefficients k_T (Nm/A) and k_F (N/A) are directly related to the magnet volume. Also, Fig. 13 shows that the radial force changes for different initial rotor angles.

Similar to Fig. 12, Fig. 13 plots radial force versus suspension current, but when the motor works under its nominal motoring conditions. These results demonstrate a linear relationship between force and current magnitude, but as anticipated from the distorted circles in Fig. 9, the curves for $\gamma = 0°$ and $\gamma = 90°$ do not overlap in Fig. 13.

Figure 14 shows the destabilizing passive radial force versus per unit radial deflection of the rotor in the x-direction. For the design D_1, the difference between the passive radial

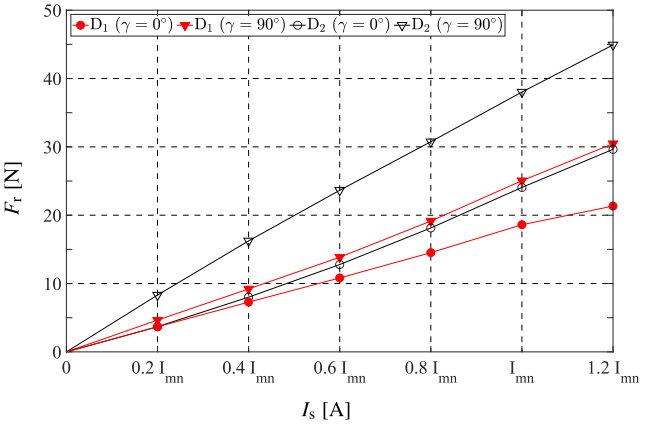

FIGURE 12. Suspension force F_r at $\theta_z = 0°$ versus suspension current I_s with $\gamma = 90°$ for zero motoring current, $I_m = 0$. The nominal suspension current is $I_{sn} = 2.23$ A.

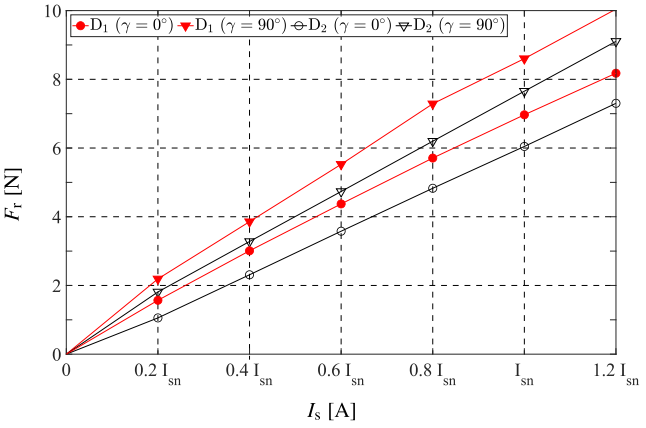

FIGURE 13. Suspension force F_r at $\theta_z = 0°$ versus suspension current I_s with $\gamma = 90°$ for nominal motoring current, $I_m = I_{mn} = 11.15$ A. The nominal suspension current is $I_{sn} = 2.23$ A.

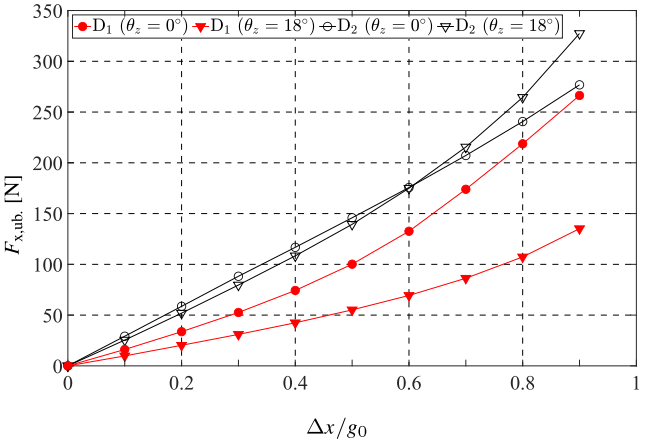

FIGURE 14. Passive radial force on the rotor at $\theta_z = 0°$ due to deflection in the radial direction x.

force for the rotor tooth aligned in the x-direction and for the rotor tooth aligned in the y-direction increases significantly at higher eccentricities, whereas for the design D_2, the effect of the rotor angle on the passive radial force is weaker. Also, as expected, increasing the magnet volume in the design

D_2 results in a higher destabilizing radial force compared to the D_1 design. The near-origin force–displacement characteristic can be approximated by a linear stiffness because the two opposite air gaps remain nearly symmetric and the magnetic circuit operates away from pronounced local saturation. A compact PM-biased representation expresses the net radial force as the difference of Maxwell-stress contributions from the two opposite air gaps $g_0 - r$ and $g_0 + r$,

$$F_r(r) \approx \frac{A_g \mu_0}{2} \left[\frac{\left(\mathcal{F}_{PM} + \mathcal{F}_c\right)^2}{(g_0 - r)^2} - \frac{\left(\mathcal{F}_{PM} - \mathcal{F}_c\right)^2}{(g_0 + r)^2} \right], \quad (9)$$

where A_g is an effective air-gap area, $\mathcal{F}_{PM}$ is the PM bias magnetomotive force, and $\mathcal{F}_c$ is the control magnetomotive force produced by the suspension winding [35]. Equation (9) is used as an explanatory approximation (constant effective air-gap area and negligible fringing), while the reported FEM and experimental results capture geometric effects and saturation. In the near-origin region ($|r| \ll g_0$), a first-order linearization is appropriate and the local stiffness $c_r(r) = \mathrm{d}F_r/\mathrm{d}r$ can be treated as approximately constant, $c_r(r) \approx c_r(0)$. The nonlinearity could be quantified over three displacement intervals (near-origin, intermediate, and large displacement) using a chosen metric, e.g., deviation from a near-origin linear fit $\Delta F_r(r) = F_r(r) - c_r(0)\, r$ and/or the displacement-dependent stiffness $c_r(r)$. As displacement increases into an intermediate region, air-gap asymmetry makes the terms $(g_0 - r)^{-2}$ and $(g_0 + r)^{-2}$ diverge, introducing a displacement-dependent slope; in the large-displacement region, the effect is amplified because the small-gap side experiences a rapid flux-density increase and stronger position-dependent saturation, which further bends $F_r(r)$ and increases $|\Delta F_r(r)|$. Equation (9) also clarifies key design implications. Increasing magnet volume increases $\mathcal{F}_{PM}$, which increases the force-per-control-MMF around the center and can therefore expand the near-origin linear region (as observed for D_2 relative to D_1 in Fig. 14) because the same suspension force can be achieved with a smaller $\mathcal{F}_c$ and reduced saturation-induced curvature. At the same time, the passive position stiffness increases with $\mathcal{F}_{PM}$, which increases the restoring-force sensitivity to displacement and implies that a larger active force margin is required to restore and centralize the rotor when displacement increases. The nominal air-gap g_0 also affects the onset of nonlinearity and a larger g_0 generally reduces the force sensitivity to a given absolute displacement r because the relative eccentricity r/g_0 is smaller. However, achieving a target suspension force with a larger g_0 typically requires a higher excitation level (larger $\mathcal{F}_{PM}$ and/or $\mathcal{F}_c$), and at larger $|r|$ the smaller-gap side can experience a pronounced flux-density increase and local saturation, which amplifies the large-displacement nonlinearity. Consequently, in wide-air-gap topologies (e.g., temple-type slice motors), the larger available clearance and the higher required excitation can make the large-displacement nonlinear region more relevant for practical suspension-force regulation.

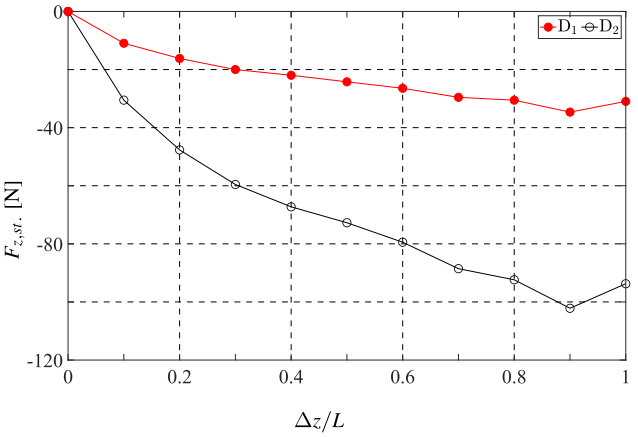

FIGURE 15. Passive axial reluctance force versus normalized axial deflection of the optimized designs.

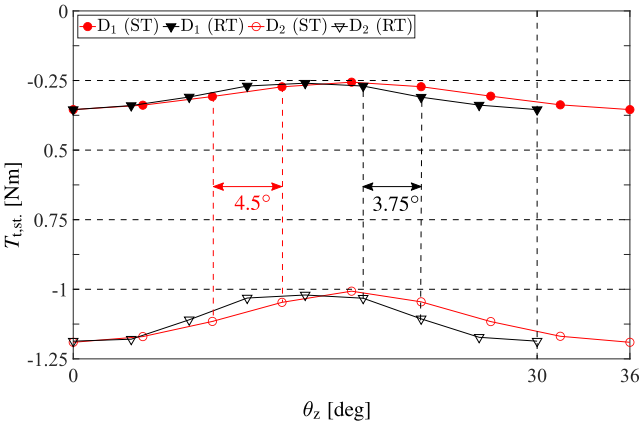

FIGURE 16. Passive tilting torque versus rotor angle of the optimized designs.

Consistent with practical operation, the nominal clearance is therefore selected so that the expected rotor motion remains within the near-origin linear region, as also supported by the experimental results (Fig. 20).

Figure 15 shows passive axial reluctance force versus normalized axial deflection for designs D_1 and D_2. The passive axial reluctance force caused by an axial displacement is mostly independent of the rotor angle, and here, it is shown for $\theta_z = 0$. Figure 15 shows that the passive axial stabilizing force and the axial stiffness are directly affected by the magnet volume.

Figure 16 shows the passive tilting torque versus the rotor angle for a tilting angle of $\Delta\theta_t = 3°$ in two tilting scenarios: (a) stationary (static) tilting (ST) with constant tilting motions in x and y axes ($\Delta\theta_x = 0°$ and $\theta_y = 3°$), (b) rotating (dynamic) tilting (RT) with variable tilting motions in x and y axes ($\Delta\theta_x = \sin(\theta_z) \cdot 3°$ and $\Delta\theta_y = \cos(\theta_z) \cdot 3°$). It can be seen that the average stabilizing tilting torque and its variation have a direct relation with the magnet volume in both scenarios. Also, it is clear that the effect of the tilting angle direction on tilting torque is negligible.

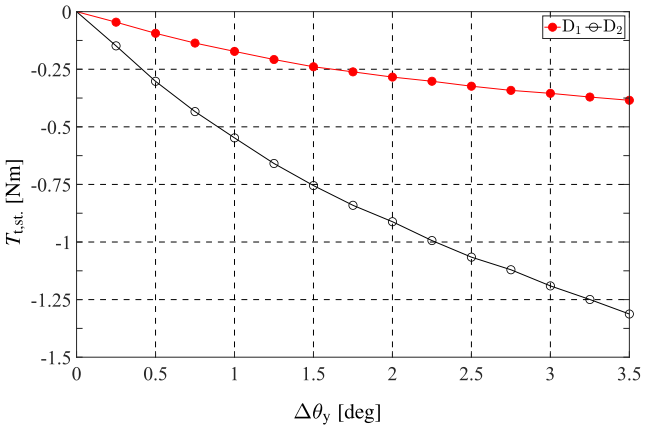

FIGURE 17. Passive tilting torque versus tilting angle of the optimized designs for tilting in *y*-direction.

Tilting stiffness can be obtained from results plotted in Figure 17 when the tilting angle changes from 0° to 3.5°, showing that design D_2 has approximately 3.5 times higher tilting stiffness compared to design D_1.

A commonly accepted and equitable measure used for comparing the torque generation of different drives is the shear stress τ. It can be formulated as

$$\tau = \frac{T_e|_{I_m=I_{mn}}}{A_r \cdot R_r} \tag{10}$$

for a rotor with the outer radius R_r, the axial rotor height d_r, and the lateral surface area of the rotor $A_r = 2\pi R_r d_r$. According to the data obtained from 3D FEM analysis for the torque generated by nominal motor current (D_1: $T_e|_{I_m=I_{mn}} = 1.071$ Nm, D_2: $T_e|_{I_m=I_{mn}} = 2.014$ Nm), $\tau_1 = 7.6$ kN/m^2 for design D_1 and $\tau_2 = 12.3$ kN/m^2 for design D_2. Results verify the significant superiority of the proposed BS-PS-FSPM motor in torque generation compared to existing FSPM slice motors and other bearingless slice motors with magnet-free rotors [36], [37]. Another key characteristic of a bearingless motor is the capability to generate suspension force. Similar to the shear-stress definition, the thrust stress can be given as

$$\sigma = \frac{F_r|_{I_s=I_{sn}}}{S_r} = \frac{F_r|_{I_s=I_{sn}}}{D_r d_r}, \tag{11}$$

where F_r is the radial suspension force, D_r is the rotor diameter, and $S_r = D_r d_r$ is the lateral cross-sectional area of the rotor. According to the data obtained from 3D FEM analysis for the radial force generated by nominal suspension current (D_1: $F_r|_{I_s=I_{sn}} = 6.645$ N, D_2: $F_r|_{I_s=I_{sn}} = 7.071$ N), $\sigma_1 = 7.016$ kN/m^2 for design D_1 and $\sigma_2 = 6.912$ kN/m^2 for design D_2.

C. EXPERIMENTAL RESULTS

This subsection presents static measurement results to verify the proposed concept. To mitigate small-scale manufacturing challenges (coils and air gap), a larger BS-PS-FSPM demonstrator with a separated single-layer winding was built, as shown in Fig. 18; although not dimensionally identical

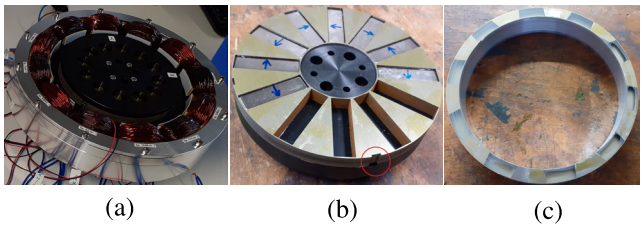

FIGURE 18. Prototype components with key geometric dimensions $R_i = 30$ mm, $R_o = 133$ mm, $W_r = 12$ mm, $W_y = 12$ mm, $H_m = 49$ mm, $W_t = 21$ mm, $W_c = 16$ mm, $W_h = 3$ mm, $\alpha_{ri} = 16°$, $\alpha_{ro} = 20°$, $d_r = d_s = 11$ mm, $g_0 = 1.5$ mm, and $\tau_{so} = 0.43$: (a) stator assembly, comprising the outer wound stator and the inner PM stator, (b) inner PM stator with the red circle indicating the position sensor location, and (c) rotor.

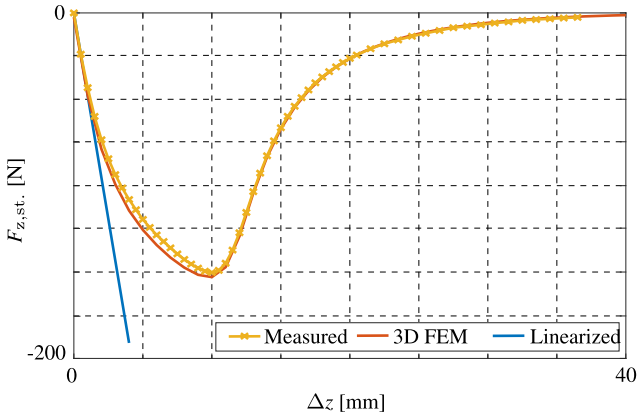

FIGURE 19. Passive axial reluctance force versus axial deflection ($\alpha_d = 0°$).

to the studied designs, it implements the same bearingless operating principles and serves to validate the concept [38]. It was assembled on a test rig equipped with an *xyz*-table. The stator was secured to a force cell on the stationary side of the table, while the rotor, linked to a torque gauge, was installed on a bearing. The rotor side of the rig was positioned on the movable part of the table.

Initial tests were conducted to evaluate the passive properties of the new design. Figure 19 illustrates the axial restoring forces observed during rotor deviations from the zero-force position, demonstrating the dependence of axial stiffness on the axial position of the rotor. The results are obtained from both FEM simulations (red curve) and experimental measurements (yellow curve). A linear approximation (blue curve) around the origin position revealed an axial stiffness of 47.8 N/mm for minor deviations. The maximum axial restoring forces were observed at $z = 10$ mm, attributed to an axial overlap of 1 mm between the rotor and the stators.

Moreover, Fig. 20 demonstrates that radial destabilizing forces were also recorded as the rotor shifted radially from the zero-force origin position. These destabilizing forces were found to be linearly related to the radial displacement, exhibiting a negative radial stiffness of -290.4 N/mm. However, this linear relationship was only valid near the origin position, with nonlinearity observed near the

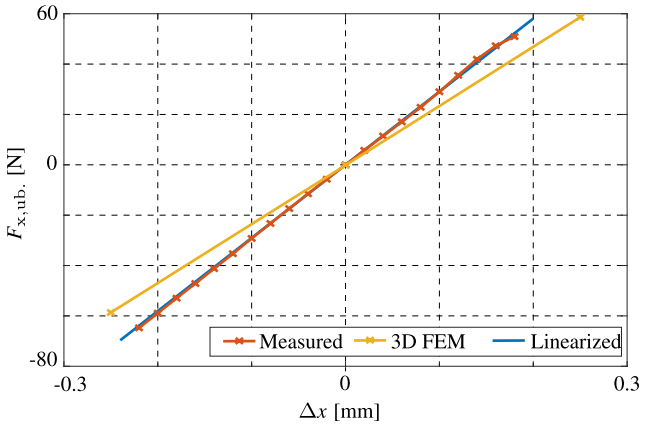

FIGURE 20. Passive radial force on the rotor at $\theta_z = 0°$ due to deflection in the radial direction x ($\alpha_d = 0°$).

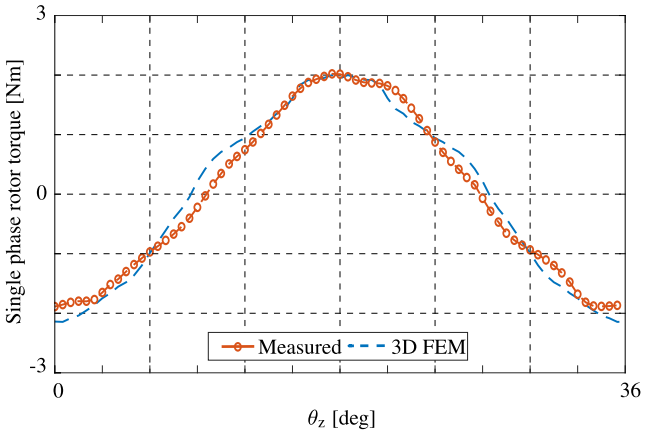

FIGURE 21. Single-phase torque characteristics ($\alpha_d = 0°$).

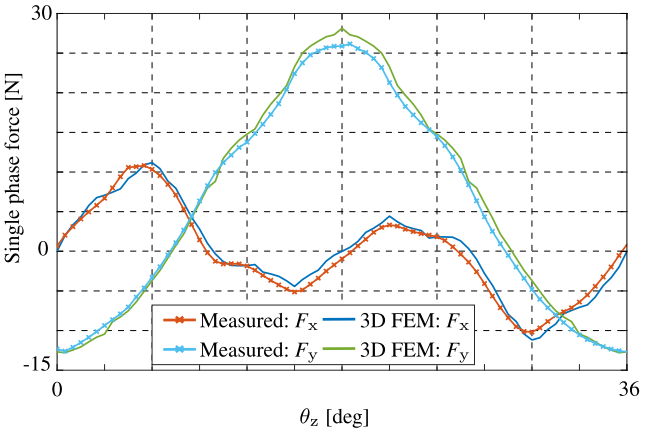

FIGURE 22. Single-phase xy-force characteristics ($\alpha_d = 0°$).

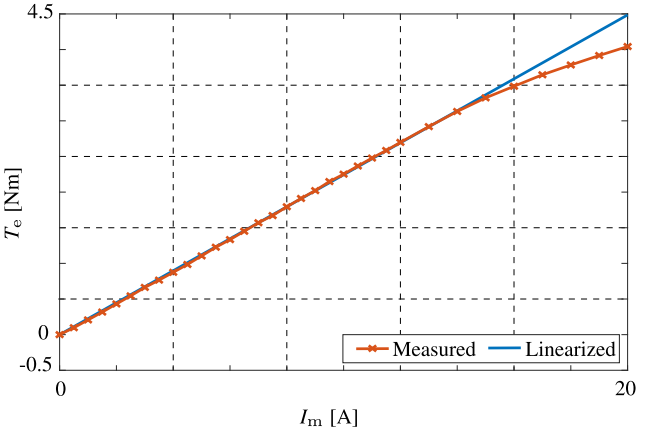

FIGURE 23. Electromagnetic torque at $\theta_z = 0°$ versus motoring current for zero suspension current ($\alpha_d = 0°$).

maximum deviation. It should be noted that the current setup did not allow the measurement of the tilt stiffness.

Figures 21 and 22 show the single-phase characteristics of the motor at a 36° mechanical angle (corresponding to a 360° electrical angle), providing the maximum suspension force and torque at the rated phase currents, as obtained from both measurements and 3D FEM simulations. The single-phase characteristics can be used to derive the complete machine characteristics (in the operating point) with reasonable accuracy. The force magnitude plot in Fig. 22 follows a trend similar to that of the single-phase torque in Fig. 21. However, the force components in Fig. 22 point to the presence of force amplitude variation and force vector error angle. Those can be shown to relate to the magnitude and phase stability measures of the closed-loop suspension control. The suspension force curves were plotted at a phase current of 1.5 A, while the drive torque was plotted at 8.5 A. The bearing force in the x-direction exhibits a second-harmonic component. Both the radial bearing force and drive torque reach their maximum at a mechanical rotor angle of 18° (equivalent to an electrical angle of 180° for a 10-rotor-pole topology), achieving a suspension force of 26.2 N and a drive torque of 2 Nm.

Figure 23 presents the peak drive torque of the single-phase characteristic as a function of the motoring phase current at a mechanical rotor angle of 0°. For comparison, the curve was linearized at the origin, indicating substantial reserves before saturation. Saturation effects first became noticeable at a phase current of 14 A, permitting a current 58.8% above nominal before saturation. The resulting current density at saturation was 7.9 A/mm^2, which is acceptable for passively air-cooled coils of a small power prototype.

In Figs. 24 and 25, a quantitative example is presented to illustrate the changes in torque and force characteristics caused by inner-stator rotation. For $\alpha_d = -15°$, the measured maximum torque is 2.23 Nm at $I_m = 8.5$ A, whereas the measured maximum bearing force is 18.31 N at $I_s = 1.5$ A. Considering the measurement uncertainty, it is also noted that, for this specific design, the 3D FEM results predict a similar peak torque value and waveform under the same single-phase arrangement. In contrast, the peak suspension force for $\alpha_d = 0°$ is higher than that for $\alpha_d = -15°$, as shown in Fig. 26. However, although the torque waveforms are similar, the suspension-force waveforms exhibit clear differences. Specifically, for $\alpha_d = -15°$, the magnitude of

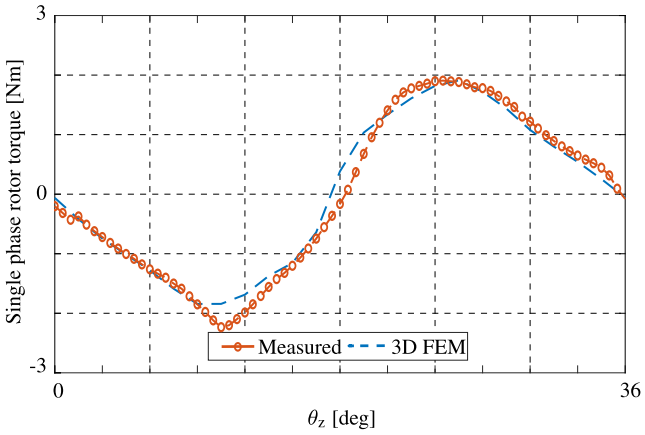

FIGURE 24. Single-phase torque characteristics ($\alpha_d = -15°$).

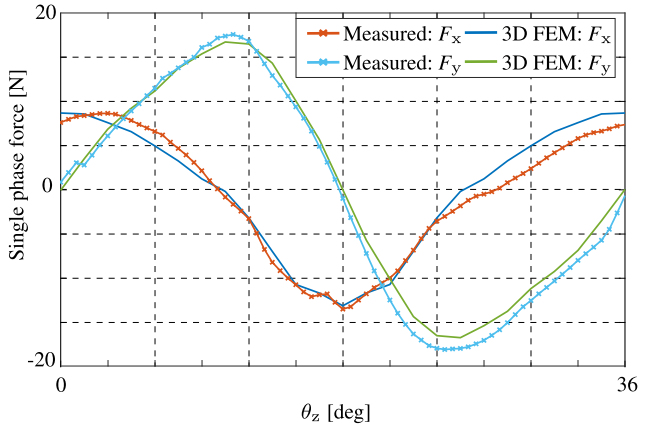

FIGURE 25. Single-phase *xy*-force characteristics ($\alpha_d = -15°$).

the suspension force is less affected, and the deviation angle of the force vector is reduced because the corresponding x- and y-components more closely follow sinusoidal and cosinusoidal forms, as observed in Fig. 25 in comparison with Fig. 22. The winding scheme for $\alpha_d = -15°$ was not investigated separately in this paper; instead, the same winding scheme as that used for $\alpha_d = 0°$ was adopted for comparison.

To enable a direct comparison between the proposed slice motor and existing designs, the shear stresses of the prototype systems, computed using (10), are plotted as a function of the lateral rotor surface in Fig. 27. Lines of constant shear force are included as visual guides for interpreting the results. It should be noted that none of the surveyed bearingless slice motors employ dedicated cooling, which can substantially influence the achievable torque density [36].

Typical shear-stress ranges for common machine classes are reported in [39]. Completely enclosed, fan-cooled industrial motors typically exhibit 1–15 kN/m^2, depending on rated power, and smaller machines generally reach lower values than larger ones. High-performance industrial servo drives commonly fall in the range of 10–20 kN/m^2, while very large liquid-cooled machines can reach approximately

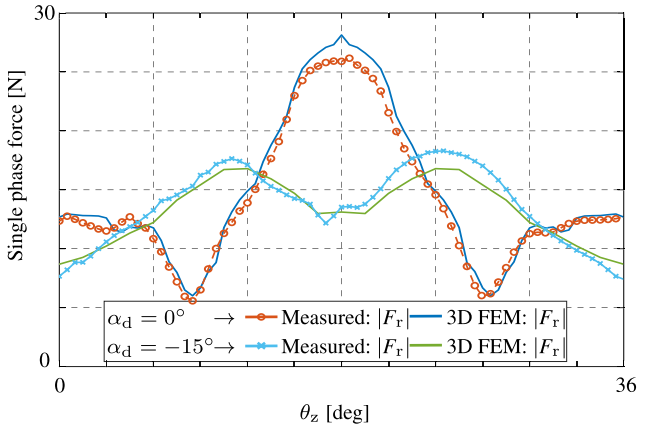

FIGURE 26. Single-phase radial force characteristics for $\alpha_d = 0°$ and $\alpha_d = -15°$.

70–100 kN/m^2. The results in Fig. 27 indicate that bearingless slice motors can attain shear stresses close to 25 kN/m^2, which is comparable to conventional electrical drives using mechanical bearings. Within the surveyed slice-motor concepts, the highest shear-stress values (exceeding 15 kN/m^2) are achieved by temple-type motor systems, which benefit from a larger available constructional space and winding window area, enabling higher electric loading. As shown in Fig. 27, the value for the prototype is 7.9 kN/m^2, where the corresponding three-phase torque is estimated from the single-phase value by applying the factor $3\sqrt{2}/2$, yielding $(3\sqrt{2}/2) \times 2.02 = 4.285$ Nm. In designs D_1 and D_2, the ratio of motoring ampere-turns to suspension ampere-turns is 5, whereas for the prototype this ratio is 1. If a similar ampere-turn ratio is considered for D_2, its value becomes $12.3 \times 3/5 = 7.98$ kN/m^2; for D_1, it becomes $7.6 \times 3/5 = 4.56$ kN/m^2. This indicates that the designs are broadly proportional under the same ampere-turn allocation, while also reflecting the lower amount of PM material in D_1.

The thrust-stress values calculated from (11) for all surveyed slice-motor systems (with a maximum of 150 kN/m^2) are summarized in Fig. 28. Temple motors also exhibit high thrust-stress values for the same reasons discussed for shear stress. In addition, the bearingless homopolar reluctance slice motor (with a magnet-free rotor) achieves thrust stress above 110 kN/m^2, indicating a strong suspension-force capability per unit surface area [36]. As shown in Fig. 28, the value for the prototype is 29.84 kN/m^2, where the corresponding three-phase force is estimated from the single-phase value by applying the factor $3\sqrt{2}/2$, yielding $(3\sqrt{2}/2) \times 26.17 = 55.5$ N. As in the torque comparison, the same ampere-turn ratio is considered for a consistent comparison. Under this condition, the value of D_2 becomes $7.07 \times 3 = 21.21$ kN/m^2, whereas that of D_1 becomes $6.91 \times 3 = 20.73$ kN/m^2. This indicates that the designs remain broadly proportional under the same ampere-turn allocation, given that the suspension force is mainly reluctance-driven and the effect of PM volume is minor.

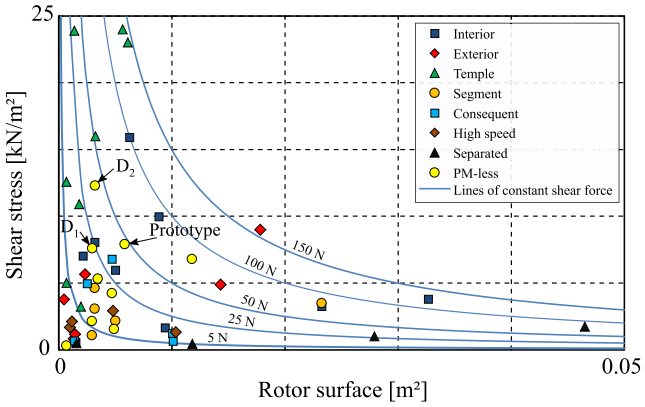

FIGURE 27. Comparison of shear stress values.

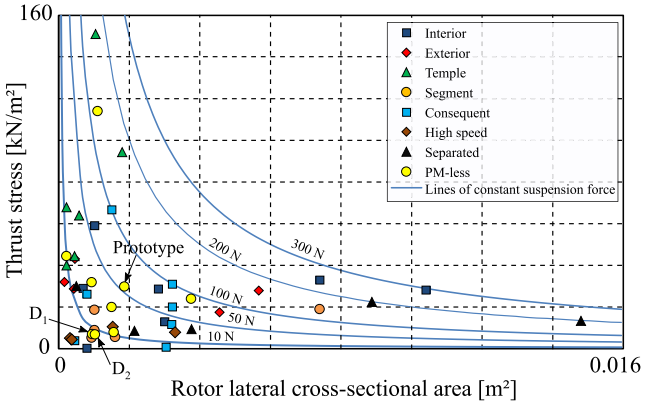

FIGURE 28. Comparison of thrust stress values.

V. CONCLUSION

This work proposes a bearingless partitioned-stator flux-switching permanent-magnet slice motor and evaluates its electromagnetic torque production and passive suspension characteristics. The presented optimization-related observations, literature-based comparison, and prototype results serve as supporting evidence to substantiate the evaluation of the proposed concept within this scope. A 12-slot/10-pole topology with separated stator parts for magnets and windings was analyzed using 2D FEM and subsequently verified using 3D models, with emphasis on steady-state torque and radial-force characteristics within the investigated operating range. The results indicate that the torque and radial-force characteristics exhibit approximately linear current dependence in the considered range, suggesting that local linearization around an operating point is reasonable for subsequent control-oriented modeling. Experimental results obtained from a prototype with a separated single-layer winding show good agreement with the corresponding 3D simulation results for torque and force characteristics, thereby providing experimental verification of combined torque production and bearingless operation for the investigated prototype configuration. Detailed controller synthesis and stability-margin analysis are outside the scope of this paper and are identified as future work. Future work will address dynamic levitation control and extended experimental characterization under a wider set of operating conditions.

REFERENCES

[1] R. P. Jastrzebski, D. Kepsu, A. Putkonen, I. Martikainen, A. Zhuravlev, and S. Madanzadeh, "Competitive technology analysis of a double stage kinetic compressor for 0.5 MW heat pumps for industrial and residential heating," in *Proc. IEEE Int. Electr. Mach. Drives Conf. (IEMDC)*, Hartford, CT, USA, May 2021, pp. 1–7.

[2] T. Nussbaumer, P. Karutz, F. Zurcher, and J. W. Kolar, "Magnetically levitated slice motors—An overview," *IEEE Trans. Ind. Appl.*, vol. 47, no. 2, pp. 754–766, Mar. 2011.

[3] B. Warberger, R. Kaelin, T. Nussbaumer, and J. W. Kolar, "50-N·m/2500-W bearingless motor for high-purity pharmaceutical mixing," *IEEE Trans. Ind. Electron.*, vol. 59, no. 5, pp. 2236–2247, May 2012.

[4] H. Mitterhofer, B. Mrak, and W. Amrhein, "Suitability investigation of a bearingless disk drive for micro turbine applications," in *Proc. IEEE Energy Convers. Congr. Expo.*, Denver, CO, USA, Sep. 2013, pp. 2480–2485.

[5] C. M. Zingerli, I. Coray, J. Weber, T. Nussbaumer, and J. W. Kolar, "Scaling of magnetically levitated homopolar hollow-shaft machines," in *Proc. IEEE 10th Int. Conf. Power Electron. Drive Syst. (PEDS)*, Kitakyushu, Japan, Apr. 2013, pp. 54–59.

[6] S. Huwyler, D. Schrag, R. Gilbert, T. Thorsen, R. Schöb, and J.-H. Hahn, "Bearingless in-line viscometer for the semiconductor industry," in *Proc. IEEE Sensors*, Oct. 2003, pp. 1077–1081.

[7] K. Asami, A. Chiba, M. A. Rahman, T. Hoshino, and A. Nakajima, "Stiffness analysis of a magnetically suspended bearingless motor with permanent magnet passive positioning," *IEEE Trans. Magn.*, vol. 41, no. 10, pp. 3820–3822, Oct. 2005.

[8] H. Sugimoto, M. Miyoshi, and A. Chiba, "Low speed test in two-axis actively positioned bearingless machines with non-collocated structure for wind power applications," in *Proc. IEEE Energy Convers. Congr. Expo. (ECCE)*, Montreal, QC, Canada, Sep. 2015, pp. 799–804.

[9] H. Bleuler, H. Kawakatsu, W. Tang, W. Hsieh, D. K. Miu, Y. Tai, F. Mösner, and M. Rohner, "Micromachined active magnetic bearings," in *Proc. 4th Int. Symp. Magn. Bearings (ISMB)*, Aug. 1994, pp. 349–352.

[10] N. Barletta and R. Schöb, "Design of a bearingless blood pump," in *Proc. 3rd Int. Symp. Magn. Suspension Technol. (ISMST)*, 1996, pp. 265–274.

[11] S. Silber, H. Grabner, R. Lohninger, and W. Amrhein, "Design aspects of bearingless torque motors," in *Proc. 13th Int. Symp. Magn. Bearings (ISMB)*, Aug. 2012, pp. 1–12.

[12] H. Onuma and T. Masuzawa, "Evaluation of magnetic suspension characteristics and levitation performance of a centrifugal blood pump using radial-type self-bearing motor," in *Proc. 14th Int. Symp. Magn. Bearings (ISMB)*, 2014, pp. 174–179.

[13] W. Gruber, J. Passenbrunner, G. Bramerdorfer, and W. Amrhein, "Novel bearingless segment motor design with axial magnetized rotor magnets," in *Proc. 8th Int. Conf. Power Electron. ECCE Asia*, May 2011, pp. 2225–2232.

[14] J. Asama, T. Tatara, T. Oiwa, and A. Chiba, "A two-axis actively regulated consequent-pole bearingless motor with wide magnetic gaps," in *Proc. IEEE Energy Convers. Congr. Expo.*, Sep. 2013, pp. 1541–1546.

[15] D. Steinert, T. Nussbaumer, and J. W. Kolar, "Evaluation of one- and two-pole-pair slotless bearingless motors with toroidal windings," *IEEE Trans. Ind. Appl.*, vol. 52, no. 1, pp. 172–180, Jan. 2016.

[16] T. Schneeberger, T. Nussbaumer, and J. W. Kolar, "Magnetically levitated homopolar hollow-shaft motor," *IEEE/ASME Trans. Mechatronics*, vol. 15, no. 1, pp. 97–107, Feb. 2010.

[17] W. Gruber and K. Radman, "Modeling and realization of a bearingless flux-switching slice motor," *Actuators*, vol. 6, no. 2, p. 12, Mar. 2017.

[18] W. Gruber, W. Briewasser, and W. Amrhein, "Novel bearingless slice motor design with four concentrated coils featuring a unique operational behaviour," in *Proc. 14th Eur. Conf. Power Electron. Appl. (EPE)*, 2011, pp. 1–10.

[19] W. Gruber, M. Rothböck, and R. T. Schöb, "Design of a novel homopolar bearingless slice motor with reluctance rotor," *IEEE Trans. Ind. Appl.*, vol. 51, no. 2, pp. 1456–1464, Mar. 2015.

[20] M. Noh, W. Gruber, and D. L. Trumper, "Hysteresis bearingless slice motors with homopolar flux-biasing," *IEEE/ASME Trans. Mechatronics*, vol. 22, no. 5, pp. 2308–2318, Oct. 2017.

[21] J. Rao, W. Hijikata, and T. Shinshi, "A bearingless motor utilizing a permanent-magnet-free structure for disposable centrifugal blood pumps," *J. Adv. Mech. Design, Syst., Manuf.*, vol. 9, no. 3, pp. 1–16, 2015.
[22] M. Sokolov, W. Gruber, S. E. Saarakkala, and M. Hinkkanen, "Modeling of a bearingless synchronous reluctance motor with combined windings," in *Proc. IEEE Energy Convers. Congr. Expo. (ECCE)*, Baltimore, MD, USA, Sep. 2019, pp. 7084–7090.
[23] A. Khamitov, W. Gruber, G. Bramerdorfer, and E. L. Severson, "Comparison of combined winding strategies for radial nonsalient bearingless machines," *IEEE Trans. Ind. Appl.*, vol. 57, no. 6, pp. 6856–6869, Nov. 2021.
[24] M. Cheng, W. Hua, J. Zhang, and W. Zhao, "Overview of stator-permanent magnet brushless machines," *IEEE Trans. Ind. Electron.*, vol. 58, no. 11, pp. 5087–5101, Nov. 2011.
[25] Z. Q. Zhu, "Switched flux permanent magnet machines—Innovation continues," in *Proc. Int. Conf. Electr. Mach. Syst.*, Aug. 2011, pp. 1–10.
[26] W. Gruber, W. Bauer, and K. Radman, "Comparison of homopolar and heteropolar bearingless reluctance slice motor prototypes," *Proc. Inst. Mech. Eng., I, J. Syst. Control Eng.*, vol. 231, no. 5, pp. 339–347, May 2017.
[27] D. J. Evans and Z. Q. Zhu, "Novel partitioned stator switched flux permanent magnet machines," *IEEE Trans. Magn.*, vol. 51, no. 1, pp. 1–14, Jan. 2015.
[28] R. P. Jastrzebski, P. Jaatinen, and O. Pyrhönen, "Modeling and control design simulations of a linear flux-switching permanent-magnet-levitated motor," *Mech. Eng. J.*, vol. 4, no. 5, pp. 1–12, 2017.
[29] N. Turk, N. Bulic, and W. Gruber, "Nonlinear control of a bearingless flux-switching slice motor with combined winding system," *IEEE/ASME Trans. Mechatronics*, vol. 25, no. 1, pp. 152–163, Feb. 2020.
[30] S. Madanzadeh, W. Gruber, A. Zhuravlev, and R. P. Jastrzebski, "Self-bearing partitioned stator flux-switching permanent magnet motor," in *Proc. 25th Int. Conf. Electr. Mach. Syst. (ICEMS)*, Nov. 2022, pp. 1–6.
[31] J. T. Chen and Z. Q. Zhu, "Winding configurations and optimal stator and rotor pole combination of flux-switching PM brushless AC machines," *IEEE Trans. Energy Convers.*, vol. 25, no. 2, pp. 293–302, Jun. 2010.
[32] A. Chiba, T. Fukao, O. Ichikawa, M. Oshima, M. Takemoto, and D. G. Dorrell, *Magnetic Bearings and Bearingless Drives*. Amsterdam, The Netherlands: Elsevier, 2005.
[33] R. P. Jastrzebski, P. Jaatinen, O. Pyrhönen, and A. Chiba, "Design optimization of permanent magnet bearingless motor using differential evolution," in *Proc. IEEE Energy Convers. Congr. Expo. (ECCE)*, Portland, OR, USA, Sep. 2018, pp. 2327–2334.
[34] A. Zhuravlev, A. Putkonen, S. Madanzadeh, and R. P. Jastrzebski, "Linear parameter-varying and fixed-parameter H_∞-based control of a bearingless compressor," *IEEE Access*, vol. 12, pp. 104344–104353, 2024.
[35] X. Sun, Z. Xue, J. Zhu, Y. Guo, Z. Yang, L. Chen, and J. Chen, "Suspension force modeling for a bearingless permanent magnet synchronous motor using Maxwell stress tensor method," *IEEE Trans. Appl. Supercond.*, vol. 26, no. 7, pp. 1–5, Oct. 2016.
[36] W. Gruber, *Bearingless Slice Motor Systems Without Permanent Magnetic Rotors* (Advances in Mechatronics), no. 45. Linz, Austria: Trauner Verlag, 2019.
[37] K. Radman, N. Bulic, and W. Gruber, "High-torque bearingless flux-switching slice drive," in *Proc. 15th Int. Symp. Magn. Bearings (ISMB)*, 2016, pp. 446–453.
[38] S. Mallinger, S. Madanzadeh, R. Jastrzebski, and W. Gruber, "Implementing a bearingless separated-stator flux-switching slice motor," in *Proc. IEEE Energy Convers. Congr. Expo. (ECCE)*, Nashville, TN, USA, Oct. 2023, pp. 3859–3866.
[39] T. J. E. Miller, *Brushless Permanent-Magnet and Reluctance Motor Drives*. Oxford, U.K.: Oxford Science Publications, 1989.

SADJAD MADANZADEH received the B.S. degree in electrical engineering from the University of Zanjan, Zanjan, Iran, in 2010, and the M.S. degree in electrical engineering from the K. N. Toosi University of Technology, Tehran, Iran, in 2013. He is currently pursuing the D.Sc. degree in electrical engineering at Lappeenranta–Lahti University of Technology, Lappeenranta, Finland. His research interests include electric drive control, electrical machine design, and power electronics.

WOLFGANG GRUBER (Senior Member, IEEE) received the Dipl.-Ing. (M.Sc.) degree in mechatronics and the Dr.techn. (Ph.D.) degree in technical sciences from Johannes Kepler University (JKU), Linz, Austria, in 2004 and 2009, respectively.

Since 2012, he has been an Assistant Professor, since 2018, an Associate Professor, and since 2021, a Full Professor with the Institute of Electrical Drives and Power Electronics, JKU. Since 2004, he has also been a Senior Researcher with the Research and Development Company, Linz Center of Mechatronics GmbH (LCM), Linz. He has developed the bearingless segment motor, reluctance motor, flux-switching motor, and PM Vernier motor. His research interests include new topologies for bearingless slice motors, their design, setup, and control. He was a recipient of the International Nagamori Award, in 2015.

STEFAN MALLINGER (Graduate Student Member, IEEE) received the B.Sc. and Dipl.-Ing. (M.Sc.) degrees in mechatronics from Johannes Kepler University Linz (JKU), Austria, in 2021 and 2023, respectively. He is currently a Graduate Teaching Assistant with the Institute of Electric Drives and Power Electronics, JKU. His research interests include magnetic gears, magnetic bearings, and bearingless drives of various topologies, in particular the bearingless induction machine.

RAFAL P. JASTRZEBSKI (Senior Member, IEEE) received the M.Sc. degree in electronics from the Technical University of Lodz, Lodz, Poland, in 2002, and the D.Sc. degree in electrical engineering from Lappeenranta–Lahti University of Technology (LUT), Lappeenranta, Finland, in 2007. From 2009 to 2011, he was a Postdoctoral Researcher with the Academy of Finland, and from 2013 to 2018, he was an Academy of Finland Research Fellow. He has held research positions in Poland, Germany, Japan, and Finland. From 2020 to 2025, he was a Docent in modeling and control of electromechanical systems at LUT. In 2023, he joined the Automation Group, Department of Mechanical Engineering, University of Turku, Turku, Finland, where he is currently an Associate Professor and the Head of the M.Sc. and Ph.D. Majors in Automation. His research interests include the design and control of electric machines, with emphasis on bearingless motors, magnetic bearings, torque and thrust dense machines, electrification, model-based control, and power systems.

NIKO NEVARANTA received the B.Sc., M.Sc., and D.Sc. degrees in electrical engineering from Lappeenranta–Lahti University of Technology, Lappeenranta, Finland, in 2010, 2011, and 2016, respectively. He is currently an Associate Professor of industrial informatics. His research interests include data-driven modeling and control of electrical drives, system identification, parameter estimation, and diagnostics. His research interests also include control approaches for active magnetic bearings and methods for rotordynamics identification.